ACS APPLIED MATERIALS & INTERFACES

www.acsami.org

Research Article

Effects of Ionic Liquid Nanoconfinement on the CO_2/CH_4 Separation in Poly(vinylidene fluoride)/1-Ethyl-3-methylimidazolium Thiocyanate Membranes

Farzin Rahmani, Paul Scovazzo, Melissa A. Pasquinelli, and Sasan Nouranian*

Cite This: *ACS Appl. Mater. Interfaces* 2021, 13, 44460−44469

Read Online

ACCESS | Metrics & More | Article Recommendations

ABSTRACT: A combined experimental and molecular dynamics (MD) simulation approach was used to investigate the effects of the nanoconfinement of a highly CO_2/CH_4-selective ionic liquid (IL), 1-ethyl-3-methylimidazolium thiocyanate ([EMIM][SCN]), in porous poly(vinylidene fluoride) (PVDF) matrices on the gas separation performance of the resulting membranes. The observed experimental CO_2/CH_4 permselectivity increased by about 46% when the nominal pore diameter in PVDF, which is a measure of nanoconfinement, decreased from 450 to 100 nm, thus demonstrating nanoconfinement improvements of gas separation. MD simulations corroborated these experimental observations and indicated a suppression in the sorption of CH_4 by [EMIM][SCN] when the IL nanoconfinement length decreased within the nonpolar PVDF surfaces. This is consistent with the experimental observation that the CH_4 permeance through the IL confined in nonpolar PVDF is significantly less than the CH_4 permeance through the IL confined in a water-wetting polar formulation of PVDF. The potential of mean force calculations further indicated that CO_2 has more affinity to the nonpolar PVDF surface than CH_4. Also, a charge/density distribution analysis of the IL in the PVDF-confined region revealed a layering of the IL into [EMIM]- and [SCN]-rich regions, where CH_4 was preferentially distributed in the former and CO_2 in the latter. These molecular insights into the nanoconfinement-driven mechanisms in polymer/IL membranes provide a framework for a better molecular design of such membranes for critical gas separation and CO_2 capture applications.

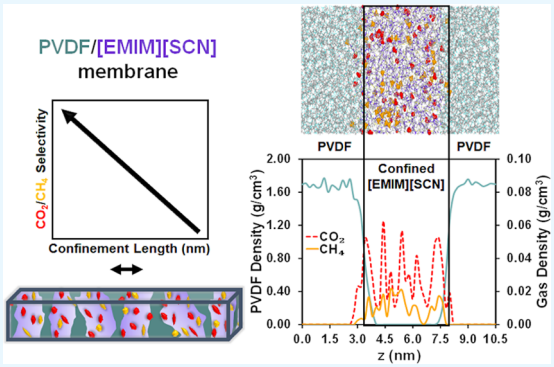

KEYWORDS: *poly(vinylidene fluoride), ionic liquid, 1-ethyl-3-methylimidazolium thiocyanate, membrane, nanoconfinement, molecular dynamics simulation, SILM, CO_2/CH_4 separation*

INTRODUCTION

Ionic liquids (ILs) have excellent potential applications in separation science and technology due to their favorable physicochemical properties, such as low vapor pressure, high thermal and chemical stability, high ionic conductivity, and good separation performance.[1] Consequently, ILs and their polymer derivatives[2] have been investigated in both supported and unsupported membrane systems.[3] In IL-based material systems, nanosized IL domains can be encapsulated or confined by an inorganic or organic matrix.[4] More often than not, this "nanoconfinement" gives rise to improved physical performance, such as enhanced thermal stability,[5−10] increased gas absorption,[11−17] or gas sorption selectivity.[18,19]

Many researchers have investigated the IL nanoconfinement phenomenon in various encapsulant materials, such as carbon nanotubes,[20−22] graphitic nanopores,[23,24] activated carbon,[25] ceramic (ZrO_2-TiO_2) films,[26] silica slits/pores,[14,27] mica,[28] metal−organic frameworks (MOFs),[29] Nafion,[30] or other porous matrices,[31] through experimental and/or computational means. Despite these efforts, experimental observations of nanoconfined ILs have remained a significant challenge. This is mainly because of enormous difficulties in creating well-defined experimental platforms with internal nanoconfined regions.[26,32] While IL gels are good platforms for nanoconfinement studies in, for example, electrochemical applications,[33] they are unstable in pressure-driven gas membrane separations.[34] Of the nanoconfinement platforms studied for gas separation applications, researchers have noted that advanced nanostructures are likely to form when, for example, block copolymers meet ILs under the affinity of the selected block with the selected IL.[26,35,36] However, a pressure-stable, tunable platform for investigating polymer-confined ILs for gas

Received: July 12, 2021
Published: September 8, 2021

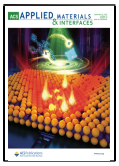

https://doi.org/10.1021/acsami.1c13169
ACS Appl. Mater. Interfaces 2021, 13, 44460−44469

separations will need a functional understanding of the nanoconfinement size effect on separation performance.

Previous experimental studies of the IL nanoconfinement effects on gas separation performance have varied widely in focus and application of interest, with no clear consensus on the ramifications of IL nanoconfinement.[32,37] For example, some studies report an increase in permeability and solubility of CO_2 and other gases in ILs confined in pores with sizes ranging from nanometer to micrometer.[37−40] Moreover, some researchers report that changing the chemistry of the confining material can increase the CO_2 permeability by a factor of 2, even when the confining pore diameters and the IL type are held constant.[38,39] The literature verdict on the impact of nanoconfinement on CO_2 selectivity is not as clear cut, with reports of improvements in selectivity[40] mixed in with reports of no improvement in selectivity.[38] Nevertheless, a brief survey of the literature on the effect of IL nanoconfinement on gas separation performance in IL-based platforms is warranted.

Recent work by Khakpay et al.[41] revealed a threefold increase in CO_2/CH_4 selectivity for 1-ethyl-3-methylimidazolium thiocyanate ([EMIM][SCN]) confined in a porous cellulose acetate (CA) matrix versus the IL homogenously dispersed in the CA film. Previous molecular dynamics (MD) simulations of the confinement of 1-butyl-3-methylimidazolium thiocyanate ([BMIM][SCN]) in MOFs predicted order-of-magnitude differences in CO_2/N_2 selectivity depending on the hydrophobicity of the confining surface.[42] Grünauer et al.[43] investigated the CO_2/N_2 separation using three different ILs and three different confining porous supports. According to their study, [EMIM] [bis(trifluoromethylsulfonyl)imide] ([EMIM][Tf_2N]) had a 50% selectivity increase in an alumina support (20 nm pores) versus that of a polystyrene-*block*-poly(4-vinylpyridine) (PS-*b*-P4VP) diblock copolymer (17 nm pores); however, there was no significant change in the selectivities of [EMIM][dicyanamide] ([EMIM][DCA]) nor [BMIM][acetate] ([BMIM][Ac]) between these two supports of equivalent pore sizes. In contrast, all three ILs had higher permeabilities in the alumina versus copolymer support.[43] When comparing the same polymer support with different pore sizes (17 nm versus 40 nm pores), none of the three ILs had a significant change in selectivity.[43] An interesting result from their work is that CO_2 permeabilities increase in the larger pores for [EMIM][DCA] (250% increase) and [BMIM][[Ac] (100% increase) but not for [EMIM][Tf_2N].[43] In contrast, Close et al.[37] found that CO_2 permeability increased by a factor of 2 when nanoconfinement in alumina changed from 20 to 100 nm. They reported that even though the permeability increases with increasing pore size, the confined permeabilities were still significantly greater than those in unconfined ILs.[37]

There are also a number of experimental and computational studies of IL phase change under nanoconfinement. For example, Banu et al.[26] reported that the melting point of a confined IL may be suppressed depending on the IL chemistry. Interestingly, some studies have determined that ILs can behave as either a liquid or a solid when in contact with solid interfaces.[44] For example, Gupta et al.[9] reported a 20 °C increase in the glass transition temperature (T_g) of [EMIM]-[ethyl sulfate] ([EMIM][$EtSO_4$]), immobilized in a silica matrix, compared to the bulk IL. Also, they reported that the thermal stability of the IL increases upon nanoconfinement.[9] They claim that these changes are due to the interactions between the SiO_2 pore wall surface, the IL cations, and anions.[9] Recently, Wang et al.[45] published a review of anomalies of ionic and molecular transport under nanoconfinement.

Overall, the root cause of the nanoconfinement phenomenon seems to be the IL-matrix interfacial interactions, leading to local ordering and orientation of the IL molecules near the interface.[46] The resulting supramolecular and structural layering, as well as changes in the dynamics of the near-interfacial region versus that of the bulk IL domain, may underlie the observed physical performance of the system. However, more research is needed to fully understand the nanoscale changes in confined ILs and the interplay between the IL and IL-confining phase interactions, molecular ordering, and charge distribution of the IL in the nanoconfined regions.

In our work, a combined experimental and MD simulation approach was used to investigate the IL nanoconfinement effects on the CO_2/CH_4 separation in (PVDF)/[EMIM]-[SCN] membranes. PVDF, both in its hydrophilic and hydrophobic variants, is used as the confinement matrix for [EMIM][SCN], a highly CO_2/CH_4-selective IL.[47] Encapsulation of ILs by a continuous matrix is an enabling approach for utilizing ILs for CO_2 absorption.[48−50] Moreover, among IL-encapsulating materials, polymers have widespread use in a variety of separation platforms. For example, fluoropolymers have traditionally been used as the continuous matrix in IL polymeric gel membranes.[51] Herein, the following hypotheses were made about the gas permeability selectivity (also referred to as permselectivity) of ILs, specifically for CO_2 separation from CH_4. First, permselectivity is a function of nanoconfinement length on the order of ∼100 nm. Second, the permselectivity improvement is also a function of the polarity of the confining surface. Because of the difficulties in creating cross-membrane pressure-stable IL films for gas separations, a hybrid experimental/MD simulation plan was more appropriate to test these hypotheses. Our experimental plan tested [EMIM][SCN] confined in PVDF pores ranging from 100 to 450 nm. The complimentary MD simulation study of the PVDF-confined [EMIM][SCN] assisted in the interpretation of the experimental results. Specifically, MD simulation explored the PVDF-IL interactions, as well as the structural layering of the IL driven by these interactions. These energetic and structural outcomes resulted in variations of molecular properties, e.g., gas solubility and diffusivity, that manifested as nanoconfinement effects on permselectivity. Given the importance of polymer/IL membranes in gas separations, especially CO_2 capture processes, a molecular-level understanding of the IL nanoconfinement phenomenon and its implications on the gas species mass transport, thermodynamics, and other physicochemical properties of the system provides a path for a more informed design of these platforms. This would enable the optimization of gas separation performance in these systems.

EXPERIMENTAL METHODS

Materials. Ultra-high-purity compressed gases of CO_2, CH_4 (purity > 99.97%), and N_2 (purity ∼ 99.998%) were acquired from nexAir Co. (Memphis, TN). [EMIM][SCN] (purity > 99.0%, CAS 331717-63-6, molar volume = 1.52×10^{-4} m^3/mol, MW = 169.25 g/mol) was purchased from IOLITEC Inc. (Tuscaloosa, AL). [EMIM][SCN] has low CH_4 solubility and, hence, produces IL membranes with high selectivities for gases being separated from CH_4.[41,52]

The stabilized IL membranes (SILMs) fabricated in this study were dual-layer membranes with a lower porous support, also known as membrane backing, and an upper transport controlling layer. The

https://doi.org/10.1021/acsami.1c13169
ACS Appl. Mater. Interfaces 2021, 13, 44460−44469

porous hydrophobic/oleophobic backing layer was Versapor-200TR (thickness = 79 μm, nominal pore size = 0.2 μm, Pall Corporation). The pores of this backing layer were not filled with the IL. Also, the IL did not wet the pores. The upper membrane transport controlling layer was a stabilized liquid layer, made by filling the pores of porous PVDF filter membranes (Millipore Corp.) with [EMIM][SCN]. Three different PVDF filter membranes were used depending on whether the objective was to test the impact of nanoconfinement length or confining surface polarity. Specifically, the PVDF filter membranes were 450 nm nominal pore size (Millipore, Cat No. HVLP04700), 100 nm nominal pore size hydrophilic confining surfaces (Millipore, Cat No. VVLP04700), and 100 nm nominal pore size hydrophobic confining surfaces (Millipore, Cat No. VVHP04700). All three PVDF membrane filters had 47 mm diameters, thicknesses of 127 μm, and 70% porosity. Additional technical information on the PVDF filters is available from the manufacturer's website. Millipore distinguishes between the two different formulations of their PVDF filter membranes by designating them either as hydrophilic or hydrophobic to qualify the ease of wetting the pores with water. Since our study did not involve water, IL membranes created from these PVDF membrane filters are referred to as either "polar surface confinement" (hydrophilic PVDF) or "nonpolar surface confinement" (hydrophobic PVDF). Some authors divide ILs into water-miscible and water-immiscible categories using the terms hydrophilic and hydrophobic. In these cases, the terms speak to the thermodynamics of the IL/water systems and not necessarily the surface chemistry of the IL.

Fabrication of the SILMs. The following was the procedure for fabricating the IL membranes by combining [EMIM][SCN] with the PVDF filter membranes: (1) 0.5 mL of [EMIM][SCN] was dripped on a watch glass to wet an area equal to the size of the PVDF membrane; (2) the PVDF membrane was placed on top of the dripped [EMIM][SCN] with the active (shiny) side facing down; (3) the porous PVDF was allowed to soak up the [EMIM][SCN]; (4) the remaining 0.5 mL was spread over the exposed side of the PVDF membrane for a total of 1 mL; (5) the watch glass and IL membrane were placed in a vacuum desiccator overnight for degassing and dehydration; (6) the excess liquid was removed from the surfaces of the IL membrane by blotting gently with filter paper; and (7) the IL membrane was installed in the membrane testing unit, on top of a Versapor-200TR, with the active side facing the higher pressure side of the membrane unit.

Apparatus. The experiments determined mixed-gas selectivities and gas permeances using a continuous flow apparatus (Figure 1). A complete description of this apparatus is given in previous work by Scovazzo et al.,[38] with the following being a brief summary:

The apparatus was inside a box used to keep the temperature at 30 °C. MKS Type 1179A Mass-Flo controllers (MFCs), operating on a molar basis, controlled the flow rates of individual gases (CO_2, CH_4, and N_2 as the sweep gas), which allowed setting the gas flow rates to a desired value or to a desired CO_2/CH_4 ratio. The mixed-gas feed was

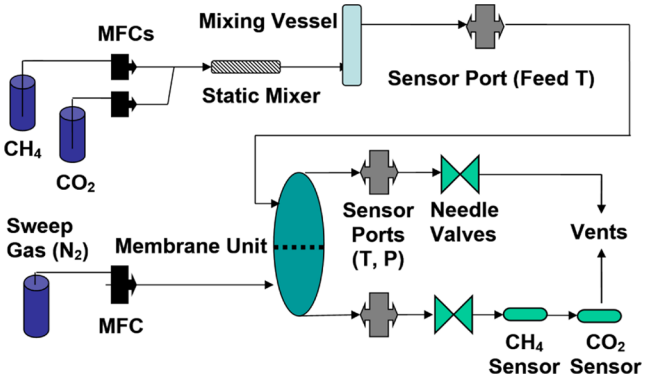

Figure 1. Diagram of the continuous flow apparatus for mixed-gas feed permeance tests.[38]

10.0 sccm CO_2 and 90.0 sccm CH_4, resulting in a feed of 10 vol % CO_2 and 90 vol % CH_4. The sweep gas was 8.0 sccm N_2. As illustrated in Figure 1, the feed stream entered an OMEGA FMX8400 Series static mixer (after passing through the flow controllers) to completely mix the gases. To achieve a stabilized and thermally equilibrated mixture, the gas then entered a 300 mL mixing vessel. After the mixing vessel, the gas flowed into the membrane unit. The well-mixed conditions on both sides of the membrane unit were achieved by impingement flows onto the center of the membrane in both the retentate and permeate chambers. The active transport area for the tested membranes was 9.62 cm^2.

The apparatus has sensors to measure the temperatures and pressures of the retentate and permeate streams. The CO_2 and CH_4 concentrations were obtained using Vaisala GMM 221 (0−5% by volume) and Edinburgh Instruments iRcel 2179 (0−5% by volume) sensors, respectively. The accuracy and performances of both infrared gas sensors were checked using calibration gases.

A computer data acquisition program recorded the mixed-gas permeance/selectivity results. The recorded data included (1) the atmospheric, retentate, and permeate pressures, (2) retentate and permeate temperatures, (3) permeate relative humidity, and (4) permeate gas concentrations (CO_2 and CH_4). Data recording occurred only after the achievement of steady-state conditions (>2 h after a feed condition change). Next, data were recorded at 1 min intervals for 1 h to ensure the achievement of steady-state conditions. The data analysis to convert the recorded data into gas permeances and mixed-gas selectivities is detailed elsewhere.[38,41]

Water content is an important consideration when studying transport phenomena in ILs. For example, the viscosity of the IL decreases with increasing water content, leading to greater gas permeability solely due to increased molecular diffusion in the liquid and not any nanoconfinement effect.[53] For this reason, experimental protocols were used to ensure negligible water content in the ILs during the gas flux measurements. These protocols included overnight membrane conditioning in a vacuum desiccator prior to placement in the experimental apparatus (Figure 1). The feed gases in the apparatus were completely dry. A relative humidity (rH) sensor in the permeate gas tracked the water content in the system. Recording of the transport data did not occur until a steady-state condition of ≤4% rH was achieved to ensure a constant negligible IL water content.

Membrane Terminology. The definition of selectivity in a rate-based separation, such as membrane processes, is the ratio of the driving-force-normalized transport rates of the faster fluxing species divided by the lower fluxing species.

$$S^{P}_{CO_2/CH_4} = \frac{P_{CO_2}}{P_{CH_4}} \quad (1)$$

where $S^{P}_{CO_2/CH_4}$ is the permselectivity of CO_2 versus CH_4 and P_x is the permeance of species x (CO_2 or CH_4) in mol/(m^2 kPa_x s). Permselectivity in IL membranes is a function of solubility selectivity, S_{CO_2/CH_4}, and diffusivity selectivity, $S^{D}_{CO_2/CH_4}$[54]

$$S^{P}_{CO_2/CH_4} = S_{CO_2/CH_4} S^{D}_{CO_2/CH_4} \quad (2)$$

where $S^{D}_{CO_2/CH_4}$ is the ratio of the molecular diffusivities of species x (CO_2 or CH_4) in the IL and S_{CO_2/CH_4} is the ratio of the gas solubilities (mol/m^3) in the IL. For CO_2 separations, IL membrane permselectivity is dominated by the IL solubility selectivity.[38] Herein, the experimental data refer to mixed-gas permselectivities. The computational data, however, report solubility selectivities, diffusivity selectivities, and permselectivities. Moreover, the experimental permeances were assumed to reflect gas transport through the IL phase, with gas transport through the parallel PVDF transport pathway assumed negligible due to the low permeabilities of gases in polymers compared to ILs. The following illustrates this assumption using literature values for gas transport through PVDF films: CO_2 permeability of 2.11 Barrers (1 Barrer = 10^{-10} cm^3(STP) cm/(cm^2s cmHg)) and CO_2/CH_4 selectivity of 26.[55] The lowest determined CO_2 permeability for the SILMs in our study was 120 Barrers,

https://doi.org/10.1021/acsami.1c13169
ACS Appl. Mater. Interfaces 2021, 13, 44460−44469

meaning that for SILMs with 70% porosity, the permeability of the CO_2 in the PVDF is <0.5% of the total SILM CO_2 permeability. Alternatively stated, transport through the liquid phase represents >99.5% of the total CO_2 transport.

COMPUTATIONAL METHODS

Molecular Models. Three different molecular models were created with the SCIENOMICS MAPS Software Suite (MAPS version 4.2) to investigate the IL nanoconfinement effect on CO_2/CH_4 separation using MD simulation: (1) bulk [EMIM][SCN], (2) nanoconfined PVDF/[EMIM][SCN] with a small confinement length of ∼2.4 nm (designated as PVDF/[EMIM][SCN]-S), and (3) nanoconfined PVDF/[EMIM][SCN] with a larger confinement length of ∼4.5 nm (PVDF/[EMIM][SCN]-L). While the nanoconfinement lengths selected for these models were smaller than the nominal PVDF pore diameters used in the experiments, the effects of nanoconfinement on CO_2/CH_4 separation and the relevant trends were comparable. The reader should also note that the term "nominal" pore size relates to the size of particles that would be rejected by the PVDF membranes if used as filters. The membranes have a distribution of actual pore sizes that include pores smaller than the stated nominal pore size.

Both of the nanoconfined systems correspond to nonpolar PVDF formulations (hydrophobic PVDF). As for the bulk [EMIM][SCN] system, 150 ionic pairs were packed in a simulation cell with a target density of 0.8 g/cm^3. For the nanoconfined systems, 35 chains of PVDF (chemical formula: $-(C_2H_2F_2)_n-$), comprised of 30 monomers (n = 30), were packed on either side of a core [EMIM][SCN] layer in a simulation cell (size: 50 × 50 × 250 Å^3). In the core IL layer, two different numbers of ionic pairs, i.e., 150 and 400, were packed to yield two nanoconfinement lengths of ∼2.4 and ∼4.5 nm, respectively, after the systems were equilibrated.

Thermal Equilibration of the Systems. All MD simulations were performed using the polymer consistent force field (PCFF)[56] and the LAMMPS software package.[57] This force field has previously been used for the atomistic simulations of CO_2 capture in poly(ionic liquid) membranes[58] and, therefore, is deemed suitable for simulations performed in our work. First, all systems were geometry-optimized using the Conjugate Gradient (CG) method.[59] Next, they were thermally equilibrated in three stages. First, an NPT (constant number of atoms, N; constant pressure, P; constant temperature, T) simulation was performed at 300 K and 1 atm for 1 ns. For all simulations, a time step of 1 fs was used, as well as a cutoff distance of 1.4 nm for long-range interactions and the particle−particle−particle−mesh (PPPM) method[60] for electrostatic potential calculations. Moreover, the temperature and pressure were controlled using the Nosé−Hoover thermostat and barostat, respectively. Second, a heating/cooling cycle was followed to ensure the systems were not trapped in local energy minima. For this purpose, an NPT simulation was performed at 400 K and 1 atm for 500 ps, after which the systems were cooled down to 300 K at a rate of 0.2 K/ps. Third, an NPT simulation was run for 10 ns for all systems to conclude the thermal equilibration step. To validate the equilibration and thermalization approach, the equilibrium density of the bulk [EMIM][SCN] system was calculated at 300 K (1.130 ± 0.005 g/cm^3), which closely matches the experimental value of 1.116 g/cm^3 at the same temperature.[61] The calculated average densities of the PVDF-confined ILs were 1.06 g/cm^3 for the larger confinement length (∼4.5 nm) and 1.01 g/cm^3 for the smaller confinement length (∼2.4 nm). Both of these average density values are within 10% of the bulk [EMIM][SCN] system. Based on these results, a nanoconfinement effect on the IL density was not conclusive. In Figure 2, the final snapshots of the equilibrated PVDF-confined [EMIM][SCN] systems are shown. These equilibrated systems were used for subsequent MD/Grand Canonical Monte Carlo (GCMC) and MD simulations.

Gas Separation Simulations. The NVT-MD/GCMC simulation method was used, similar to our previous work,[62] to calculate the solubility selectivity of CO_2 versus CH_4 in the three systems. NVT-MD/GCMC simulations were performed for 1 ns at 300 K and 75 kPa. In this method, the GCMC procedure was applied after each 100 MD steps, while the GCMC attempts were 1000 with 1000 MC moves. Through the above procedure, an exchange of the CO_2 and CH_4 molecules with an implicit equimolar CO_2/CH_4 reservoir takes place at the same temperature and pressure conditions. In the nanoconfined IL systems, an insertion region was defined, which extended from the PVDF-IL interface on top of the [EMIM][SCN] core layer to the bottom interface.

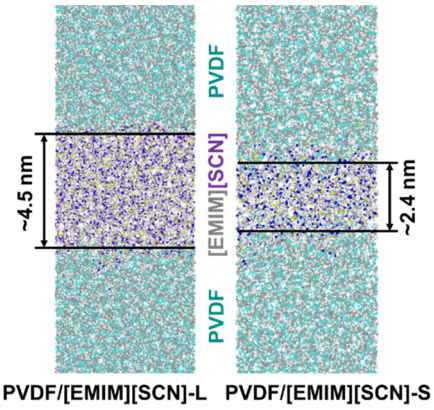

Figure 2. Final snapshots of the thermally equilibrated PVDF-confined [EMIM][SCN] systems at two different nanoconfinement lengths.

To elaborate more on the methodology used for gas separation simulations in this work, one might expect that there is an IL swelling effect because of CO_2 absorption in the IL. However, the amount of CO_2-induced IL swelling at a pressure of 75 kPa was assumed negligible in this work (<1%). This assumption was based on the experimental data for the absorption of CO_2 in [MMIM][DMP], [EMIM][DMP], and [EMIM][DEP], which was published by Wang et al.[63] At the pressure of 75 kPa, an extrapolation of the published swelling data for these ILs yield a nearly negligible swelling percentage. Therefore, by inference from these results and expecting the same behavior for [EMIM][SCN], an NVT-MD/GCMC simulation method was deemed appropriate and, hence, adopted.

Molecular Transport Simulations. The CO_2 and CH_4 diffusivities and diffusion selectivities in the three systems were calculated by separately inserting 50 CO_2 and 50 CH_4 molecules in the bulk IL and the confined IL regions and equilibrating the systems with an NVT simulation at 300 K for 9 ns. Next, during a production run of 1 ns, the trajectory data were collected every 50 ps and were used to calculate the mean-square displacement (MSD) of the CO_2 and CH_4 molecules. MSD is calculated based on the time-series of all atomic positions $\boldsymbol{r}$

$$\mathrm{MSD} \equiv \langle [\mathbf{r}(t) - \mathbf{r}(0)]^2 \rangle = \frac{1}{t} \sum_{t=t_0}^{t} [\mathbf{r}(t) - \mathbf{r}(0)]^2 \tag{3}$$

Diffusivity (D) is calculated using a linear regression fit to the MSD data for the linear portion of the curve and applying the Einstein equation[64]

$$D = \frac{1}{6} \lim_{t \to \infty} \frac{\mathrm{MSD}}{t} \tag{4}$$

Moreover, density profiles of the membrane components and gas species (bin size: 0.20 nm), as well as charge distribution in the confined regions, were generated.

Surface Affinity Calculations. Potential of mean force (PMF) calculation was performed for a single CO_2 (or CH_4) molecule approaching the interface in PVDF/[EMIM][SCN]-L. This procedure was similar to that used in our previous work.[65,66] To calculate the PMF, a single molecule of CO_2 (or CH_4) was inserted in the middle of the IL slab (x = 2.5 nm, y = 2.5 nm, and z = 5.0 nm). Next, a spring with a constant of 100 kcal/(mol Å^2) was applied to the

https://doi.org/10.1021/acsami.1c13169
ACS Appl. Mater. Interfaces 2021, 13, 44460−44469

tethered single molecule to the position of x = 2.5 nm, y = 2.5 nm, and z = 1.5 nm, which was fixed in the xy plane. The molecule was made to move in the z-direction through the PVDF/IL interface with a distance increment of 0.1 nm. At each distance increment, the NVT (constant number of atoms, N; constant volume, V; constant temperature, T) simulation was run for 100 ps to equilibrate the system. Once the distance was traversed, the PMF was calculated using the following formula:

$$\mathrm{PMF}(d) = \int_{d_1}^{d_2} \langle F(r) \rangle \mathrm{d}r \tag{5}$$

where d is the distance between the molecule's center of mass and the designated position, r is the reaction coordinate, and $\langle F(r) \rangle$ is the average spring force.

RESULTS AND DISCUSSION

Based on the literature review, the experimental plan investigated the effects of two independent variables, i.e., nanoconfinement length and polarity of the confining surfaces, on the CO_2 permeance (P_{CO_2}), CH_4 permeance (P_{CH_4}), and permselectivity. In reference to the nanoconfinement length, membranes made of PVDF-confined [EMIM][SCN] with nominal pore sizes of 100 and 450 nm were tested. The nominal refers to the size of particles rejected by the membranes when used as filters; the actual pore sizes form a distribution that includes pores smaller than the stated nominal pore size.

The nanoconfinement length test results are provided in Figure 3. These measurements indicate that the mixed-gas

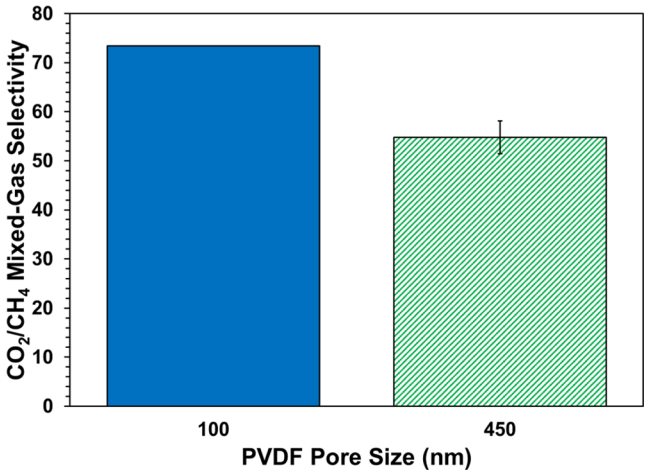

Figure 3. CO_2/CH_4 mixed-gas permselectivity as a function of PVDF pore size. The 450 nm nominal pore size data is the average of two runs with permselectivities of 52.4 and 57.2. In the case of 100 nm pore size, only the lowest quantifiable selectivity measured at a cross-membrane pressure of 65 kPa is shown.

permselectivity for the stabilized, i.e., nanoconfined, IL membrane improves with decreasing nominal pore size of the PVDF membrane. This improvement could come from an increase in membrane stability (increased capillary forces) or a nanoconfinement effect. The data are consistent with but insufficient to prove a nanoconfinement effect. However, the 100 nm permselectivity of 73 is high compared to literature values for unconfined [EMIM][SCN] of approximately 50.[41] Permselectivity quantification at 100 nm is complicated by the polarity of the PVDF pore wall. The following paragraphs and figures explore this complication. For simplicity, the lowest quantifiable selectivity measured at a cross-membrane pressure of 65 kPa is shown in Figure 3. To test the second independent variable, polarity of the confining surface, two different formulations of the 100 nm porous PVDF membranes were obtained from the same manufacturer, where one formulation is easily wetted by water (hydrophilic) and one formulation has lower polarity surfaces (hydrophobic). Using these two different PVDF formulations, two different SILMs of [EMIM][SCN] were made: one confined by polar surfaces and one confined by nonpolar surfaces. The experiments, therefore, tested the impact of the polarity of the confining surfaces while keeping the IL, confining lengths, and continuous polar phase constant.

Duplicate polar and nonpolar SILMs were made and tested. The results indicate near-identical CO_2 permeances for the membranes when the cross-membrane total pressure differences are below 165 kPa (polar = 1.03 ± 0.09 GPUs and nonpolar = 1.00 ± 0.06 GPUs). In Figure 4, representative

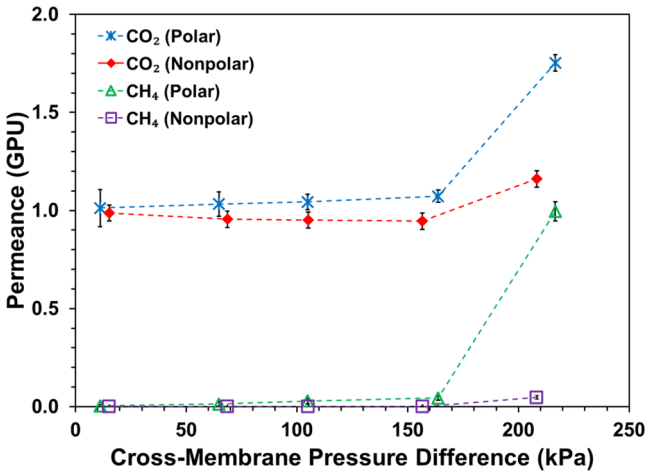

Figure 4. Gas permeances in [EMIM][SCN] SILMs, confined in PVDF supports with a nominal pore size of 100 nm. The CO_2 permeances are similar, irrelevant of the polarity of the confining surface. The rapid increase in the gas permeances above 165 kPa-diff indicates cross-membrane pressure-induced membrane instability. The dashed lines are to guide the eye only. Note: 1 GPU = 3.3467 × 10^{-10} mol/(m^2 Pa s).

CO_2 and CH_4 permeances are given over a range of cross-membrane total pressure differences. Note that there is a rapid increase in gas permeances when the cross-membrane pressure exceeds 165 kPa-diff. This type of rapid increase in gas permeances is an indication of IL displacement from the pores of the PVDF membrane and, therefore, the onset of cross-membrane-pressure-induced instability. The observed cross-membrane pressure stability limit of 165 kPa-diff in this work is consistent with that of SILMs of similar type, which has maximum cross-membrane pressure stabilities of <400 kPa-diff.[38]

Because of the much lower permeances of CH_4 versus CO_2, Figure 5 zooms in on the CH_4 permeances in Figure 4. These measurements indicate that the nonpolar membrane has significantly lower CH_4 permeances compared to those of the polar membrane at cross-membrane pressures below 165 kPa-diff. Thus, the nonpolar nanoconfinement results in higher permselectivities based on eq 1. While it is discerned that the hydrophobic nanoconfinement results in higher permselectivities, the actual permselectivity values are un-

https://doi.org/10.1021/acsami.1c13169
ACS Appl. Mater. Interfaces 2021, 13, 44460−44469

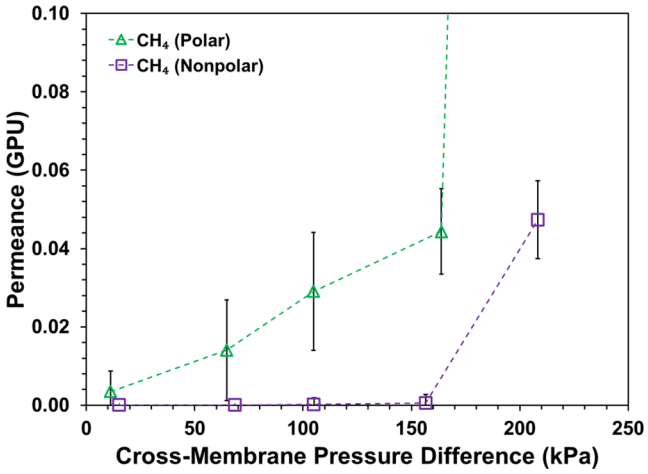

Figure 5. CH_4 permeances in [EMIM][SCN] SILMs, confined in PVDF supports with a nominal pore size of 100 nm. The CH_4 permeances are significantly lower for the IL confined in the nonpolar surface formulation of the porous PVDF support. The rapid increase in the gas permeances above 165 kPa-diff indicates cross-membrane pressure-induced membrane instability. The dashed lines are to guide the eye only. Note: 1 GPU = 3.3467×10^{-10} mol/(m^2 Pa s).

quantifiable because of the large standard-percent deviations on the CH_4 permeances. These large standard deviations resulted from the fluxes being at, or close to, the equipment detection limit (Figure 4).

The experimental observations that the permselectivity of the 100 nm pore size SILM is greater than that of the 450 nm pore size and that nanoconfinement within nonpolar surfaces results in greater permselectivity than that of polar surface confinement are consistent with the hypothesis about nanoconfinement. However, smaller pore sizes and altered surface chemistries could lead to higher capillary forces and greater cross-membrane pressure stability of the 100 nm nonpolar confined SILM compared to the polar confined or larger pore size confinement. Consequently, the experimental data are insufficient to prove the hypothesis that the benefits of nanoconfinement are a function of both nanoconfinement length and surface chemistry of the confinement. Therefore, the following discusses the computational evidence on nanoconfinement obtained from MD simulations.

MD/GCMC simulations were performed to calculate the solubility selectivities of CO_2/CH_4 (S_{CO_2/CH_4}) in the different systems and subsequently compare the gas separation performance in bulk [EMIM][SCN] versus nanoconfined PVDF/[EMIM][SCN]. The following formula was used in the MD calculation of solubility selectivity

$$S_{CO_2/CH_4} = \frac{\left(\frac{x_{CO_2}}{x_{CH_4}}\right)_{membrane}}{\left(\frac{x_{CO_2}}{x_{CH_4}}\right)_{gas\ reservoir}} \quad (6)$$

where x is the mole fraction of the species. Here, the gas reservoir refers to the implicit bulk gas pair, as used in the MD/GCMC simulations. The resulting CO_2/CH_4 solubility selectivities, diffusivity selectivities, and permselectivities of the three systems at 50 kPa are given in Table 1. The PVDF-confined IL demonstrates a 72% higher permselectivity than the bulk IL, which is consistent with the experimental

Table 1. Selectivities of CO_2/CH_4 in the Bulk and Nanoconfined IL Systems Calculated from MD/GCMC Simulations

	solubility selectivity (S_{CO_2/CH_4})[a]	diffusivity selectivity ($S^D_{CO_2/CH_4}$)[b]	permselectivity ($S^P_{CO_2/CH_4}$)[c]
Bulk [EMIM][SCN]	32	1.01	32
PVDF/[EMIM][SCN]-L[d]	43	1.29	55
PVDF/[EMIM][SCN]-S[e]	60	1.06	63

[a]Calculated using eq 6. [b]Calculated using the CO_2 and CH_4 diffusivities reported in Table 2. [c]Calculated using eq 2. [d]Nanoconfinement length: ~4.5 nm. [e]Nanoconfinement length: ~2.4 nm.

observation of a 46% higher selectivity for the PVDF-confined IL membrane (Figure 3). The simulations also illustrate a roughly 34% increase in solubility selectivity in going from no nanoconfinement to a nanoconfinement length of ~4.5 nm and then an additional 40% increase in solubility selectivity by reducing the nanoconfinement length to ~2.4 nm. Thus, a total of about 88% increase in solubility selectivity is observed in going from no confinement to the smallest confinement length. This observation suggests that a nonlinear correlation may exist between solubility selectivity and nanoconfinement length.

To gain a molecular understanding of the nanoconfinement effect on the observed solubility selectivities, the free energy profiles of the affinity of CO_2 and CH_4 for the PVDF-IL interface were generated in the nanoconfined IL region. Moreover, structural details of [EMIM][SCN] were calculated from MD simulations, including ion layering and selective path of diffusion for the CO_2 and CH_4 through these ion layers, as well as the diffusivities of CO_2 and CH_4. The PMF[67] plots, which represent how free energy changes as a function of the distance between the center of mass of the CO_2 and CH_4 species and the PVDF surface in the PVDF/[EMIM][SCN]-L system, are provided in Figure 6. These plots indicate that CO_2

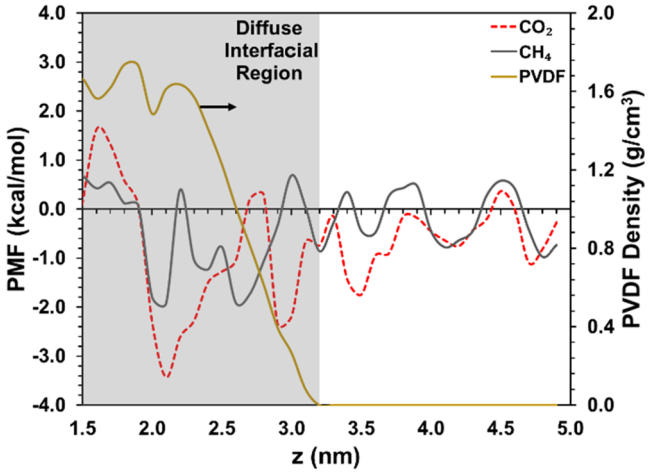

Figure 6. Potential of mean force (PMF) of CO_2 and CH_4 as a function of distance from the bulk of the nanoconfined IL region in the PVDF/[EMIM][SCN]-L system (z = 5 nm) to the diffuse PVDF-IL interfacial region (z = 1.5 nm) (shaded gray area); for reference, the PVDF density profile is also shown.

https://doi.org/10.1021/acsami.1c13169
ACS Appl. Mater. Interfaces 2021, 13, 44460−44469

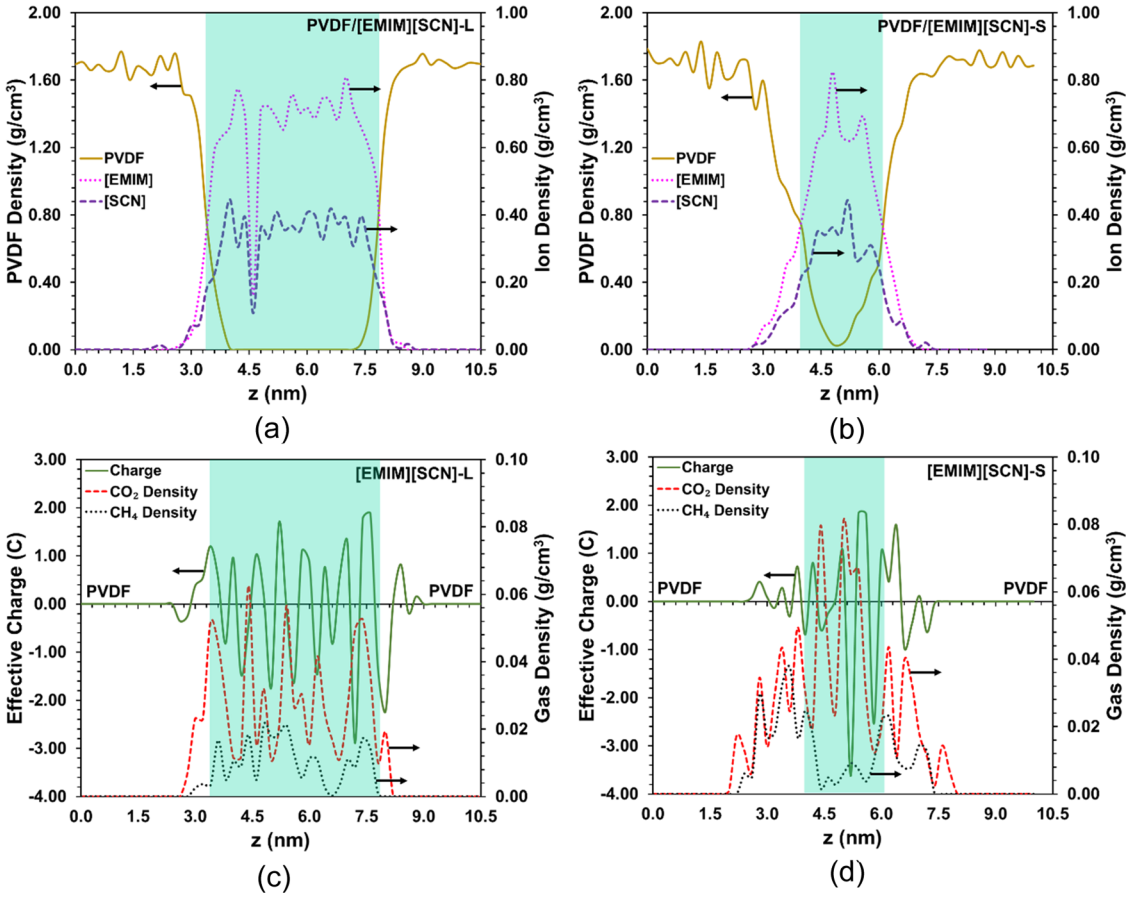

Figure 7. Density profiles of membrane components, i.e., [EMIM] cation, [SCN] anion, and PVDF in (a) PVDF/[EMIM][SCN]-L and (b) PVDF/[EMIM][SCN]-S systems. The shaded green areas represent the PVDF-confined IL regions (~4.5 nm in the PVDF/[EMIM][SCN]-L and ~2.4 nm in the PVDF/[EMIM][SCN]-S system). Effective charge distribution and gas density profiles in the PVDF-confined IL regions are also given for (c) PVDF/[EMIM][SCN]-L and (d) PVDF/[EMIM][SCN]-S systems. Comparison of the gas densities indicates a nanoconfinement-length-correlated suppression of CH_4 density versus that of CO_2.

exhibits deeper energy wells than CH_4 in the proximity of the PVDF-IL interface, revealing a higher affinity of CO_2 and lower affinity of CH_4 with the PVDF surface. The deepest well is observed within the "diffuse" PVDF-IL interfacial region, which is created because of the swelling of PVDF by the IL when thermally equilibrated. By investigating the PMF plots in Figure 6, a layered distribution of CO_2 and CH_4 in the confined IL region is discerned.

The equilibrium density profiles of the membrane components, i.e., PVDF, [EMIM] cation, [SCN] anion, and gas species, i.e., CO_2 and CH_4, in the two differently sized confined IL regions were determined from the MD trajectory data and are given in Figure 7. In both PVDF/[EMIM][SCN]-L and PVDF/[EMIM][SCN]-S systems, an interspersion of the IL, gas species, and PVDF are observed at the PVDF-IL interface, with the magnitude being higher for the confined IL region with the smaller size (PVDF/[EMIM][SCN]-S). This interspersion of membrane components and gas species is nearly symmetric and gives rise to the diffuse interfacial region mentioned before. The density profiles of both the [EMIM] cation and [SCN] anion in the confined IL region are fluctuating in intensity, which indicates ion layering (Figures 7a,b). A similar ion layering phenomenon has been observed in other confined IL systems.[68] To provide a better picture of this behavior, plots of "effective" charge distribution in the confined IL region for both systems were generated and overlaid with the CO_2 and CH_4 density profiles and are given in Figure 7c,d. The effective charge represents the total sum of the positive and negative charges of the [EMIM] cations and [SCN] anions, respectively. As a consequence of ion layering in the confined IL region, CO_2 molecules are observed to be distributed preferentially in the [SCN]-rich layers. On the contrary, CH_4 molecules distribute preferentially in the [EMIM]-rich layers. As for CO_2, its density peaks roughly coincide with valleys of the effective charge, at least within the confined region (Figure 7c,d). The smaller (more negative) effective charges are associated with the layers rich in [SCN]. It is plausible that electrostatic interactions between the CO_2 molecules and [SCN] anions are responsible for the observed CO_2 distribution pattern in the nanoconfined IL region. Similar to our observation herein, Chaban[69] reported on the key role that the [SCN] anions play in CO_2 capture in 1,3-dimethylimidazolium thiocyanate ([MMIM][SCN]) ILs. His work further suggests that the impact of the [MMIM] cation on CO_2 capture is mediocre. This observation has been contributed to the strong CO_2-[SCN] binding beyond just electrostatic interactions and involving partial sharing of valence orbitals.[69] Similarly, CH_4 molecules preferentially distributed in [EMIM]-rich layers within the confined region (Figure 7c,d), as evidenced by the CH_4 density peaks roughly coinciding with the peaks of the effective charge (more positive and, hence, [EMIM]-rich).

https://doi.org/10.1021/acsami.1c13169
ACS Appl. Mater. Interfaces 2021, 13, 44460−44469

A critical observation from Figure 7 is that the CH_4 density is suppressed in the nanoconfined IL region versus that of CO_2 for the PVDF/[EMIM][SCN]-S system and supports the experimental observation (Figure 5) of a reduction in the CH_4 permeance in the case of the IL confined in nonpolar PVDF with the nominal pore size of 100 nm. To investigate the diffusion of CO_2 and CH_4 in bulk and confined IL, the MSD of each gas species was calculated during the last 1 ns of the MD production runs and are given in Figure 8. The MSD curves for

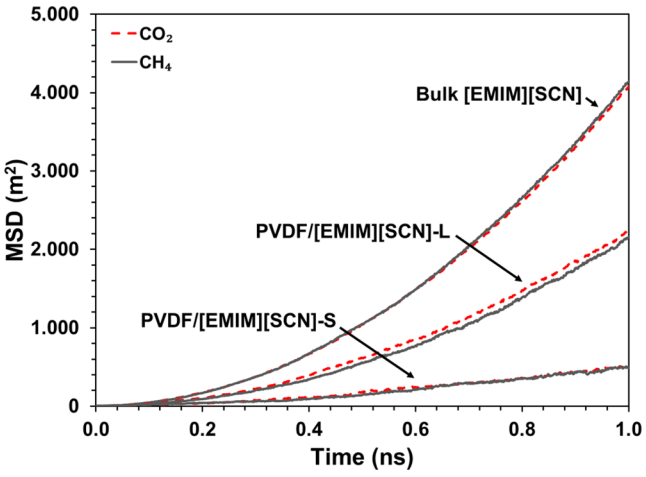

Figure 8. Mean-square displacement (MSD) of CO_2 and CH_4 as a function of simulation time for the bulk IL and PVDF-confined IL systems. The data were collected during the last 1 ns of the production runs.

CO_2 and CH_4 nearly coincide in both bulk and confined IL, suggesting that the CO_2/CH_4 separation in [EMIM][SCN] membranes is not diffusion-controlled. This observation is consistent with the reports by numerous researchers based on experimental data and is also why the permselectivity for CO_2 separation in IL membranes is solubility-selectivity-controlled.[38] Another observation from Figure 8 is that the MSD values decrease with the IL nanoconfinement within PVDF. They further decrease with a decrease in the nanoconfinement length. The average diffusivities of CO_2 and CH_4 in [EMIM][SCN] are given in Table 2.

Table 2. Diffusivities of CO_2 and CH_4 in the Bulk and PVDF-confined IL Systems Calculated from the MSD Data Using Eq 4

	D ($\times 10^{10}$ m^2/s)	
	CO_2	CH_4
bulk [EMIM][SCN]	9.38	9.32
PVDF/[EMIM][SCN]-L[a]	6.10	4.72
PVDF/[EMIM][SCN]-S[b]	3.68	3.48

[a]Nanoconfinement length: ~4.5 nm. [b]Nanoconfinement length: ~2.4 nm.

The data in Table 2 indicate that diffusivities of both CO_2 and CH_4 in [EMIM][SCN] decrease with decreasing nanoconfinement length. Similarly, based on a pulsed field gradient NMR study, Hazelbaker et al.[16] reported that the diffusivity of CO_2 in [BMIM][Tf_2N], nanoconfined in the pores of a KIT-6 silica support with a nominal pore size of 8.5 nm, decreased when compared to the CO_2 diffusivity in the bulk IL. The observed decrease in the diffusivities of CO_2 and CH_4 in the PVDF-confined [EMIM][SCN] versus those of the bulk IL is believed to be a consequence of the PVDF-IL interactions, as illustrated in Figure 6.

CONCLUSIONS

Numerous studies have reported that nanoconfinement of an IL in a polymer support (i.e., in SILMs) affects the dynamics and transport of gaseous species through the IL phase. Unfortunately, it is extremely difficult to systematically investigate the nanoconfinement phenomenon on the gas separation performance of SILMs experimentally, since it is not trivial to create well-defined polymer-confined IL regions that are stable to cross-membrane pressure differences. Therefore, this work used a combined experimental/computational approach to investigate the effects of nanoconfinement on the CO_2/CH_4 separation in a PVDF/[EMIM][SCN] SILM.

The experimental measurements of gas permeances through membranes with polar and nonpolar PVDF support and at two different nominal pore sizes of 450 and 100 nm revealed a 46% increase in the CO_2/CH_4 permselectivity in going from unconfined to PVDF-confined [EMIM][SCN] with the nominal PVDF pore size of 100 nm. For the latter, higher permselectivities were observed when the PVDF support was nonpolar (hydrophobic). The increase in the permselectivity of the nonpolar PVDF-confined IL membrane with the nanoconfinement size of 100 nm came from a reduction in the CH_4 permeance compared to the polar PVDF-confined IL with the same nanoconfinement size. However, the CO_2 permeances for 100 nm nominal pore size confinement, both polar and nonpolar, were equivalent. The increase in CO_2/CH_4 permselectivities in the PVDF-confined IL with the smaller nominal pore size over that of the bulk IL could be attributed to either a nanoconfinement effect or increased cross-membrane pressure stability (increased capillary pressures). However, MD simulations found that with decreasing nanoconfinement length, the CH_4 density is suppressed in the nonpolar PVDF-confined IL region, as opposed to the CO_2 density, corroborating the experimental observation that CH_4 permeance is reduced with a decrease in the PVDF nominal pore size to 100 nm and in going from polar to nonpolar PVDF support.

The MD simulations of bulk and nonpolar PVDF-confined ILs provided other evidence that the nonconfinement effects and not increased capillary forces are the explanation for the experimentally observed improvement in the CO_2/CH_4 separation performance. Several MD observations were made that confirmed the following: (1) CO_2/CH_4 solubility selectivity and permselectivity increase with the nanoconfinement of [EMIM][SCN] by nonpolar PVDF and with decreasing nanoconfinement length; (2) CO_2 has more affinity with the nonpolar PVDF surface than CH_4; (3) [EMIM]-[SCN] undergoes ion layering in the PVDF-confined IL regions and, hence, [EMIM]- and [SCN]-rich layers are formed in these regions at equilibrium; (4) CO_2 and CH_4 molecules distribute preferentially in the [SCN]-rich and [EMIM]-rich layers, respectively; and (5) diffusivities of CO_2 and CH_4 in [EMIM][SCN] decrease with decreasing IL nanoconfinement lengths in nonpolar PVDF. These molecular insights into the role of nanoconfinement of a highly CO_2/CH_4-selective IL, [EMIM][SCN], in the CO_2/CH_4 separation performance and molecular transport of the gaseous species through the IL provide ample evidence to back the

https://doi.org/10.1021/acsami.1c13169
ACS Appl. Mater. Interfaces 2021, 13, 44460−44469

experimental observations. Moreover, they provide a means to a better molecular design of SILMs for critical gas separation applications.

AUTHOR INFORMATION

Corresponding Author

Sasan Nouranian − *Department of Chemical Engineering, University of Mississippi, Oxford, Mississippi 38677, United States;* orcid.org/0000-0002-8319-2786; Email: sasan@olemiss.edu

Authors

Farzin Rahmani − *Department of Forest Biomaterials, North Carolina State University, Raleigh, North Carolina 27695, United States;* orcid.org/0000-0002-6321-1070

Paul Scovazzo − *Department of Chemical Engineering, University of Mississippi, Oxford, Mississippi 38677, United States;* orcid.org/0000-0003-2990-7055

Melissa A. Pasquinelli − *Department of Forest Biomaterials, North Carolina State University, Raleigh, North Carolina 27695, United States;* orcid.org/0000-0001-5815-2558

Complete contact information is available at: https://pubs.acs.org/10.1021/acsami.1c13169

Notes

The authors declare no competing financial interest.

ACKNOWLEDGMENTS

This material is based upon work supported by the National Science Foundation under Grant No. CBET-2031021. Pasquinelli and Rahmani acknowledge support from the College of Natural Resources at North Carolina State University.

REFERENCES

(1) Berthod, A.; Ruiz-Ángel, M. J.; Carda-Broch, S. Recent Advances on Ionic Liquid Uses in Separation Techniques. *J. Chromatogr. A* **2017**, *1559*, 2−16.

(2) Mecerreyes, D. Polymeric Ionic Liquids: Broadening the Properties and Applications of Polyelectrolytes. *Prog. Polym. Sci.* **2011**, *36*, 1629−1648.

(3) Noble, R. D.; Gin, D. L. Perspective on Ionic Liquids and Ionic Liquid Membranes. *J. Memb. Sci.* **2011**, *369*, 1−4.

(4) Zhang, S.; Zhang, J.; Zhang, Y.; Deng, Y. Nanoconfined Ionic Liquids. *Chem. Rev.* **2017**, *117*, 6755−6833.

(5) Neouze, M.-A.; Litschauer, M. Confinement of 1-Butyl-3-Methylimidazolium Nitrate in Metallic Silver. *J. Phys. Chem. B* **2008**, *112*, 16721−16725.

(6) Chen, S.; Kobayashi, K.; Miyata, Y.; Imazu, N.; Saito, T.; Kitaura, R.; Shinohara, H. Morphology and Melting Behavior of Ionic Liquids inside Single-Walled Carbon Nanotubes. *J. Am. Chem. Soc.* **2009**, *131*, 14850−14856.

(7) Göbel, R.; White, R. J.; Titirici, M.-M.; Taubert, A. Carbon-Based Ionogels: Tuning the Properties of the Ionic Liquid via Carbon−Ionic Liquid Interaction. *Phys. Chem. Chem. Phys.* **2012**, *14*, 5992−5997.

(8) Verma, Y. L.; Gupta, A. K.; Singh, R. K.; Chandra, S. Preparation and Characterisation of Ionic Liquid Confined Hybrid Porous Silica Derived from Ultrasonic Assisted Non-Hydrolytic Sol−Gel Process. *Microporous Mesoporous Mater.* **2014**, *195*, 143−153.

(9) Gupta, A. K.; Verma, Y. L.; Singh, R. K.; Chandra, S. Studies on an Ionic Liquid Confined in Silica Nanopores: Change in Tg and Evidence of Organic−Inorganic Linkage at the Pore Wall Surface. *J. Phys. Chem. C* **2014**, *118*, 1530−1539.

(10) Han, M.; Gu, Z.; Chen, C.; Wu, Z.; Que, Y.; Wang, Q.; Wan, H.; Guan, G. Efficient Confinement of Ionic Liquids in MIL-100 (Fe) Frameworks by the "Impregnation-Reaction-Encapsulation" Strategy for Biodiesel Production. *RSC Adv.* **2016**, *6*, 37110−37117.

(11) Zhang, J.; Zhang, S.; Dong, K.; Zhang, Y.; Shen, Y.; Lv, X. Supported Absorption of CO_2 by Tetrabutylphosphonium Amino Acid Ionic Liquids. *Chem.-Eur. J.* **2006**, *12*, 4021−4026.

(12) Zhang, J.; Zhang, Q.; Li, X.; Liu, S.; Ma, Y.; Shi, F.; Deng, Y. Nanocomposites of Ionic Liquids Confined in Mesoporous Silica Gels: Preparation, Characterization and Performance. *Phys. Chem. Chem. Phys.* **2010**, *12*, 1971−1981.

(13) Ren, J.; Wu, L.; Li, B.-G. Preparation and CO_2 Sorption/Desorption of N-(3-Aminopropyl) Aminoethyl Tributylphosphonium Amino Acid Salt Ionic Liquids Supported into Porous Silica Particles. *Ind. Eng. Chem. Res.* **2012**, *51*, 7901−7909.

(14) Shi, W.; Luebke, D. R. Enhanced Gas Absorption in the Ionic Liquid 1-n-Hexyl-3-Methylimidazolium Bis (Trifluoromethylsulfonyl) Amide ([Hmim][Tf2N]) Confined in Silica Slit Pores: A Molecular Simulation Study. *Langmuir* **2013**, *29*, 5563−5572.

(15) Khan, N. A.; Hasan, Z.; Jhung, S. H. Ionic Liquids Supported on Metal-organic Frameworks: Remarkable Adsorbents for Adsorptive Desulfurization. *Chem.-Eur. J.* **2014**, *20*, 376−380.

(16) Hazelbaker, E. D.; Guillet-Nicolas, R.; Thommes, M.; Kleitz, F.; Vasenkov, S. Influence of Confinement in Mesoporous Silica on Diffusion of a Mixture of Carbon Dioxide and an Imidazolium-Based Ionic Liquid by High Field Diffusion NMR. *Microporous Mesoporous Mater.* **2015**, *206*, 177−183.

(17) Ruckart, K. N.; O'Brien, R. A.; Woodard, S. M.; West, K. N.; Glover, T. G. Porous Solids Impregnated with Task-Specific Ionic Liquids as Composite Sorbents. *J. Phys. Chem. C* **2015**, *119*, 20681−20697.

(18) Zhang, Z.; Wu, L.; Dong, J.; Li, B.-G.; Zhu, S. Preparation and SO2 Sorption/Desorption Behavior of an Ionic Liquid Supported on Porous Silica Particles. *Ind. Eng. Chem. Res.* **2009**, *48*, 2142−2148.

(19) Li, X.; Zhang, L.; Zheng, Y.; Zheng, C. SO_2 Absorption Performance Enhancement by Ionic Liquid Supported on Mesoporous Molecular Sieve. *Energy Fuels* **2015**, *29*, 942−953.

(20) Singh, R.; Monk, J.; Hung, F. R. A Computational Study of the Behavior of the Ionic Liquid [BMIM+][PF6−] Confined inside Multiwalled Carbon Nanotubes. *J. Phys. Chem. C* **2010**, *114*, 15478−15485.

(21) Shi, W.; Sorescu, D. C. Molecular Simulations of CO_2 and H_2 Sorption into Ionic Liquid 1-n-Hexyl-3-Methylimidazolium Bis (Trifluoromethylsulfonyl) Amide ([Hmim][Tf2N]) Confined in Carbon Nanotubes. *J. Phys. Chem. B* **2010**, *114*, 15029−15041.

(22) Dou, Q.; Sha, M.; Fu, H.; Wu, G. Melting Transition of Ionic Liquid [Bmim][PF6] Crystal Confined in Nanopores: A Molecular Dynamics Simulation. *J. Phys. Chem. C* **2011**, *115*, 18946−18951.

(23) Rajput, N. N.; Monk, J.; Hung, F. R. Structure and Dynamics of an Ionic Liquid Confined inside a Charged Slit Graphitic Nanopore. *J. Phys. Chem. C* **2012**, *116*, 14504−14513.

(24) Rajput, N. N.; Monk, J.; Singh, R.; Hung, F. R. On the Influence of Pore Size and Pore Loading on Structural and Dynamical Heterogeneities of an Ionic Liquid Confined in a Slit Nanopore. *J. Phys. Chem. C* **2012**, *116*, 5169−5181.

(25) Rajput, N. N.; Monk, J.; Hung, F. R. Ionic Liquids Confined in a Realistic Activated Carbon Model: A Molecular Simulation Study. *J. Phys. Chem. C* **2014**, *118*, 1540−1553.

(26) Banu, L. A.; Wang, D.; Baltus, R. E. Effect of Ionic Liquid Confinement on Gas Separation Characteristics. *Energy Fuels* **2013**, *27*, 4161−4166.

(27) Coasne, B.; Viau, L.; Vioux, A. Loading-Controlled Stiffening in Nanoconfined Ionic Liquids. *J. Phys. Chem. Lett.* **2011**, *2*, 1150−1154.

(28) Karunaratne, W. V.; Margulis, C. J. Structure and Dynamics of an Ionic Liquid Mixture Film Confined by Mica. *J. Phys. Chem. C* **2019**, *123*, 20971−20979.

(29) Ivanov, M. Y.; Poryvaev, A. S.; Polyukhov, D. M.; Prikhod'ko, S. A.; Adonin, N. Y.; Fedin, M. V. Nanoconfinement Effects on

Structural Anomalies in Imidazolium Ionic Liquids. *Nanoscale* **2020**, *12*, 23480−23487.
(30) Sun, D.; Zhou, J. Ionic Liquid Confined in Nafion: Toward Molecular-level Understanding. *AIChE J.* **2013**, *59*, 2630−2639.
(31) Singh, M. P.; Singh, R. K.; Chandra, S. Ionic Liquids Confined in Porous Matrices: Physicochemical Properties and Applications. *Prog. Mater. Sci.* **2014**, *64*, 73−120.
(32) Vioux, A.; Coasne, B. From Ionogels to Biredox Ionic Liquids: Some Emerging Opportunities for Electrochemical Energy Storage and Conversion Devices. *Adv. Energy Mater.* **2017**, *7*, No. 1700883.
(33) Sasikumar, B.; Arthanareeswaran, G.; Ismail, A. F. Recent Progress in Ionic Liquid Membranes for Gas Separation. *J. Mol. Liq.* **2018**, *266*, 330−341.
(34) Hoarfrost, M. L.; Tyagi, M. S.; Segalman, R. A.; Reimer, J. A. Effect of Confinement on Proton Transport Mechanisms in Block Copolymer/Ionic Liquid Membranes. *Macromolecules* **2012**, *45*, 3112−3120.
(35) Tang, B.; White, S. P.; Frisbie, C. D.; Lodge, T. P. Synergistic Increase in Ionic Conductivity and Modulus of Triblock Copolymer Ion Gels. *Macromolecules* **2015**, *48*, 4942−4950.
(36) Ban, Y.; Li, Z.; Li, Y.; Peng, Y.; Jin, H.; Jiao, W.; Guo, A.; Wang, P.; Yang, Q.; Zhong, C.; et al. Confinement of Ionic Liquids in Nanocages: Tailoring the Molecular Sieving Properties of ZIF-8 for Membrane-based CO_2 Capture. *Angew. Chem. Int. Ed.* **2015**, *54*, 15483−15487.
(37) Close, J. J.; Farmer, K.; Moganty, S. S.; Baltus, R. E. CO_2/N_2 Separations Using Nanoporous Alumina-Supported Ionic Liquid Membranes: Effect of the Support on Separation Performance. *J. Memb. Sci.* **2012**, *390*−*391*, 201−210.
(38) Scovazzo, P.; Havard, D.; McShea, M.; Mixon, S.; Morgan, D. Long-Term, Continuous Mixed-Gas Dry Fed CO_2/CH_4 and CO_2/N_2 Separation Performance and Selectivities for Room Temperature Ionic Liquid Membranes. *J. Memb. Sci.* **2009**, *327*, 41−48.
(39) Chen, D.; Ying, W.; Guo, Y.; Ying, Y.; Peng, X. Enhanced Gas Separation through Nanoconfined Ionic Liquid in Laminated MoS2 Membrane. *ACS Appl. Mater. Interfaces* **2017**, *9*, 44251−44257.
(40) Tu, W.; Richert, R.; Adrjanowicz, K. Dynamics of Pyrrolidinium-Based Ionic Liquids under Confinement. I. Analysis of Dielectric Permittivity. *J. Phys. Chem. C* **2020**, *124*, 5389−5394.
(41) Khakpay, A.; Scovazzo, P.; Nouranian, S. Homogeneous and Biphasic Cellulose Acetate/Room Temperature Ionic Liquid Membranes for Gas Separations: Solvent and Phase-Inversion Casting vs. Supported Ionic Liquid Membranes. *J. Memb. Sci.* **2019**, *589*, No. 117228.
(42) Gupta, K. M.; Chen, Y.; Jiang, J. Ionic Liquid Membranes Supported by Hydrophobic and Hydrophilic Metal−Organic Frameworks for CO_2 Capture. *J. Phys. Chem. C* **2013**, *117*, 5792−5799.
(43) Grünauer, J.; Shishatskiy, S.; Abetz, C.; Abetz, V.; Filiz, V. Ionic Liquids Supported by Isoporous Membranes for CO_2/N_2 Gas Separation Applications. *J. Memb. Sci.* **2015**, *494*, 224−233.
(44) Hayes, R.; Warr, G. G.; Atkin, R. At the Interface: Solvation and Designing Ionic Liquids. *Phys. Chem. Chem. Phys.* **2010**, *12*, 1709−1723.
(45) Wang, M.; Hou, Y.; Yu, L.; Hou, X. Anomalies of Ionic/Molecular Transport in Nano and Sub-Nano Confinement. *Nano Lett.* **2020**, *20*, 6937−6946.
(46) Perkin, S. Ionic Liquids in Confined Geometries. *Phys. Chem. Chem. Phys.* **2012**, *14*, 5052−5062.
(47) Kim, J. E.; Kim, H. J.; Lim, J. S. Solubility of CO_2 in Ionic Liquids Containing Cyanide Anions:[C2Mim][SCN],[c2Mim][N-(CN)2],[c2Mim][C(CN)3]. *Fluid Phase Equilib.* **2014**, *367*, 151−158.
(48) Moya, C.; Alonso-Morales, N.; Gilarranz, M. A.; Rodriguez, J. J.; Palomar, J. Encapsulated Ionic Liquids for CO_2 Capture: Using 1-Butyl-methylimidazolium Acetate for Quick and Reversible CO_2 Chemical Absorption. *ChemPhysChem* **2016**, *17*, 3891−3899.
(49) Moya, C.; Alonso-Morales, N.; de Riva, J.; Morales-Collazo, O.; Brennecke, J. F.; Palomar, J. Encapsulation of Ionic Liquids with an Aprotic Heterocyclic Anion (AHA-IL) for CO_2 Capture: Preserving the Favorable Thermodynamics and Enhancing the Kinetics of Absorption. *J. Phys. Chem. B* **2018**, *122*, 2616−2626.
(50) Lemus, J.; Palomar, J.; Carvalho, P. J.; Coutinho, J. A. P.; et al. Solubility of Carbon Dioxide in Encapsulated Ionic Liquids. *Sep. Purif. Technol.* **2018**, *196*, 41−46.
(51) Jansen, J. C.; Friess, K.; Clarizia, G.; Schauer, J.; Izak, P. High Ionic Liquid Content Polymeric Gel Membranes: Preparation and Performance. *Macromolecules* **2011**, *44*, 39−45.
(52) Carvalho, P. J.; Coutinho, J. A. P. The Polarity Effect upon the Methane Solubility in Ionic Liquids: A Contribution for the Design of Ionic Liquids for Enhanced CO_2/CH_4 and H_2S/CH_4 Selectivities. *Energy Environ. Sci.* **2011**, *4*, 4614−4619.
(53) Seddon, K. R.; Stark, A.; Torres, M.-J. Influence of Chloride, Water, and Organic Solvents on the Physical Properties of Ionic Liquids. *Pure Appl. Chem.* **2000**, *72*, 2275−2287.
(54) Morgan, D.; Ferguson, L.; Scovazzo, P. Diffusivities of Gases in Room-Temperature Ionic Liquids: Data and Correlations Obtained Using a Lag-Time Technique. *Ind. Eng. Chem. Res.* **2005**, *44*, 4815−4823.
(55) Rajati, H.; Navarchian, A. H.; Tangestaninejad, S. Preparation and Characterization of Mixed Matrix Membranes Based on Matrimid/PVDF Blend and MIL-101 (Cr) as Filler for CO_2/CH_4 Separation. *Chem. Eng. Sci.* **2018**, *185*, 92−104.
(56) Sun, H.; Mumby, S. J.; Maple, J. R.; Hagler, A. T. An Ab Initio CFF93 All-Atom Force Field for Polycarbonates. *J. Am. Chem. Soc.* **1994**, *116*, 2978−2987.
(57) Plimpton, S. Fast Parallel Algorithms for Short-Range Molecular Dynamics. *J. Comput. Phys.* **1995**, *117*, 1−19.
(58) Fang, W.; Luo, Z.; Jiang, J. CO_2 Capture in Poly(Ionic Liquid) Membranes: Atomistic Insight into the Role of Anions. *Phys. Chem. Chem. Phys.* **2013**, *15*, 651−658.
(59) Payne, M. C.; Teter, M. P.; Allan, D. C.; Arias, T. A.; Joannopoulos, J. D. Iterative Minimization Techniques for Ab Initio Total-Energy Calculations: Molecular Dynamics and Conjugate Gradients. *Rev. Mod. Phys.* **1992**, *64*, 1045.
(60) Hockney, R. W.; Eastwood, J. W. *Computer Simulation Using Particles*; CRC Press, 1988.
(61) Larriba, M.; Navarro, P.; García, J.; Rodríguez, F. Selective Extraction of Toluene from N-Heptane Using [Emim][SCN] and [Bmim][SCN] Ionic Liquids as Solvents. *J. Chem. Thermodyn.* **2014**, *79*, 266−271.
(62) Rahmani, F.; Nouranian, S.; Chiew, Y. C. 3D Graphene as an Unconventional Support Material for Ionic Liquid Membranes: Computational Insights into Gas Separations. *Ind. Eng. Chem. Res.* **2020**, *59*, 2203−2210.
(63) Wang, J.; Petit, C.; Zhang, X.; Park, A.-H. A. Simultaneous Measurement of CO_2 Sorption and Swelling of Phosphate-Based Ionic Liquid. Green. *Energy Environ.* **2016**, *1*, 258−265.
(64) Frenkel, D.; Smit, B. *Understanding Molecular Simulation: From Algorithms to Applications*, 2nd ed.; Academic Press, 2002; pp 88−89.
(65) Rahmani, F.; Nouranian, S.; Mahdavi, M.; O'Haver, J. H. A Fundamental Investigation of the Surfactant-Stabilized Single-Walled Carbon Nanotube/Epoxy Resin Suspensions by Molecular Dynamics Simulation. *Mater. Res. Express* **2017**, *4*, No. 15016.
(66) Khakpay, A.; Rahmani, F.; Nouranian, S.; Scovazzo, P. Molecular Insights on the CH_4/CO_2 Separation in Nanoporous Graphene and Graphene Oxide Separation Platforms: Adsorbents versus Membranes. *J. Phys. Chem. C* **2017**, *121*, 12308−12320.
(67) Shih, C.-J.; Lin, S.; Strano, M. S.; Blankschtein, D. Understanding the Stabilization of Liquid-Phase-Exfoliated Graphene in Polar Solvents: Molecular Dynamics Simulations and Kinetic Theory of Colloid Aggregation. *J. Am. Chem. Soc.* **2010**, *132*, 14638−14648.
(68) Borghi, F.; Podestà, A. Ionic Liquids under Nanoscale Confinement. *Adv. Phys. X* **2020**, *5*, No. 1736949.
(69) Chaban, V. The Thiocyanate Anion Is a Primary Driver of Carbon Dioxide Capture by Ionic Liquids. *Chem. Phys. Lett.* **2015**, *618*, 89−93.

https://doi.org/10.1021/acsami.1c13169
ACS Appl. Mater. Interfaces 2021, 13, 44460−44469